NUCL SCI TECH (2021) 32:132
https://doi.org/10.1007/s41365-021-00959-y

Design optimization of 3.9 GHz fundamental power coupler for the SHINE project

Zhen-Yu Ma[1] · Jin-Fang Chen[1]

Received: 24 July 2021 / Revised: 30 September 2021 / Accepted: 21 October 2021 / Published online: 25 November 2021

Abstract The third harmonic superconducting cryomodule is being designed for the Shanghai High repetition rate XFEL and Extreme light facility (SHINE) project, which is under construction. In contrast to the European X-ray Free Electron Laser (E-XFEL) project, the 3.9 GHz cryomodules in the SHINE project will operate in the continuous wave regime with higher radio frequency average power for both cavities and couplers. We propose a 3.9 GHz fundamental power coupler with an adjustable antenna length, for satisfying the SHINE project requirements. Here, we describe the 3.9 GHz fundamental power coupler's design considerations and power requirements for various operating modes of the SHINE Linac. We also present the results of the radio frequency simulation and optimization, including the studies on multipacting and thermal analysis of the proposed 3.9 GHz coupler.

Keywords 3.9 GHz fundamental power coupler · Third harmonic cavity · Superconducting cryomodule · XFEL and extreme light facility (SHINE) Linac

This work was supported by Shanghai Municipal Science and Technology Major Project (No. 2017SHZDZX02).

✉ Jin-Fang Chen
chenjinfang@zjlab.org.cn

1 Shanghai Advanced Research Institute, Chinese Academy of Sciences, Shanghai 201204, China

1 Introduction

The Shanghai HIgh repetition rate XFEL aNd Extreme light facility (SHINE) is the first hard X-ray free electron laser facility in China, which is under construction in Shanghai Pudong New District [1–3]. The SHINE facility includes an 8-GeV-energy superconducting linear accelerator, three undulator lines, three beamlines, and the first 10 experiment stations in stage I. It will provide high-resolution imaging, ultra-fast process exploration, advanced structural analysis, and other cutting-edge research methods for research in many fields, such as physics, chemistry, life sciences, material sciences, and energy sciences. The Linac contains 600 accelerating cavities operating at 1.3 GHz, which are assembled in 75 superconducting cryomodules. It also contains 16 superconducting cavities operating at the third harmonic frequency of 3.9 GHz, which are assembled in two superconducting cryomodules. The third harmonic cryomodules are applied just before the first bunch compressor chicane in Main Linac, for linearizing the longitudinal phase space distortion before bunch compression, which is caused by the cosine-like accelerated voltage curve of the 1.3 GHz accelerating cryomodule [4–6].

The fundamental power coupler is one of the most important and complicated components of the superconducting cryomodule. Its main function is to provide microwave power to the superconducting cavity, for establishing an accelerating electric field within the cavity. Simultaneously, the ceramic windows of the couplers are also used for isolating the super-high vacuum environment in the cavity from the atmosphere [7–9]. Fermilab designed and built a power coupler for the FLASH 3.9 GHz cryomodule operating in the pulse regime (1.3 ms × 10

Hz × 45 kW; maximal average power ~ 600 W). The same 3.9 GHz coupler design is used for the E-XFEL project. The Linac Coherent Light Source facility (LCLS-II) 3.9 GHz power coupler was modified from an old FNAL/XFEL style coupler for 2 kW continuous wave (CW) average power [10, 11]. Both 3.9 GHz couplers, for the E-XFEL and LCLS-II, adopt a fixed antenna length. The E-XFEL team reported external quality factor measurements on the first 3.9 GHz cryomodule (eight cavities), which showed that the external quality factor can vary by the factor of two across cavities [12]. For the SHINE project, a 3.9 GHz fundamental power coupler was designed for the third harmonic cavity, which was developed after a series of shape optimizations [4]. The main technical parameters of the 3.9 GHz fundamental power coupler are listed in Table 1. The SHINE 3.9 GHz fundamental power coupler was designed to withstand 2 kW CW power in the traveling wave (TW) mode, and the optimal external quality factor of the third harmonic cavity was 2.13×10^7. Compared with the E-XFEL and LCLS-II 3.9 GHz power couplers, the most prominent advantage of the SHINE 3.9 GHz power coupler is that the external quality factor of the cavity can be changed by adjusting the coupler antenna insertion depth, to compensate for the tolerance caused by the cryomodule assembly [13, 14]. The adjustment range of the external quality factor spans from 1.0×10^7 to 5.0×10^7. In contrast to the layout of the 1.3 GHz couplers in the accelerating cryomodules, a 180° rotation layout is adopted between the adjacent cavities for the 3.9 GHz power couplers in the third harmonic cryomodules, for minimizing transverse radio frequency (RF) kicks caused by fundamental power couplers [15].

The remainder of this paper is organized as follows. In Sect. 2, the geometry and functionality of the SHINE 3.9 GHz fundamental power coupler, and the power requirements for different accelerator operating conditions are briefly introduced. In Sect. 3, the detailed RF simulation and optimization of the 3.9 GHz coupler are presented. In addition, the multipacting calculation and thermal analysis are presented separately in Sect. 4 and Sect. 5. Finally, the study's conclusions are presented in Sect. 6.

2 Coupler design and power requirements

The SHINE 3.9 GHz fundamental power coupler consists of four sections: (1) the cold section, (2) the warm section, (3) the waveguide-to-coax transition, and (4) the tuning mechanism. The mechanical design of the SHINE 3.9 GHz fundamental power coupler is shown in Fig. 1. The 3.9 GHz coupler adopts dual ceramic windows and a 50-Ohm-resistance coaxial line design. The cold cylindrical window is similar to the SHINE 1.3 GHz fundamental power coupler's cold window, and the warm circular window is based on the conventional window design that is developed for commercial klystrons [16]. The vacuum sides of the ceramic windows are coated with TiN, for reducing the secondary electron emission coefficient (SEC). The bellows in the inner and outer conductors are used for compensating for the mechanical flexibility and thermal shrinkage during the cryomodule assembly and cooldown. The antenna of the cold section and the waveguide-to-coax transition are made of oxygen-free copper, while the others are made of stainless steel. The hollow structure of the antenna serves to reduce the mechanical stress on the cold ceramic window. All stainless steel RF surfaces are coated with copper films for reducing the RF loss, and the thickness of the copper film on the inner conductor of the warm section was increased to 150 μm, to alleviate overheating.

There are three diagnostic ports in the 3.9 GHz coupler: two electron pickup probes are separately installed in the cold and warm sections for detecting the emission of secondary electrons, while one arc detector is installed in the waveguide-to-coax transition for detecting arcing inside the coupler. In addition, a vacuum pump port is added to the waveguide-to-coax transition, for pumping out the vacuum of the warm section. In addition, the 5 K and 45 K intercept points of the 3.9 GHz coupler are connected by a

Table 1 Main technical parameters of the SHINE 3.9 GHz fundamental power coupler

Parameters	Specification
Frequency (GHz)	3.9
Type	Coaxial, dual windows
Window type	Cylindrical (cold) + Planar (warm)
Coupler power capability (kW)	0.9 (0.1 mA beam current)
Coupler power capability (kW)	1.8 (0.3 mA beam current)
Conditioning power, TW mode (kW)	2 (test bench)
External quality factor, Q_{ext}	2.13×10^7
Q_{ext} adjustment range	$1.0 \times 10^7 \sim 5.0 \times 10^7$
Antenna adjustment range (mm)	± 3

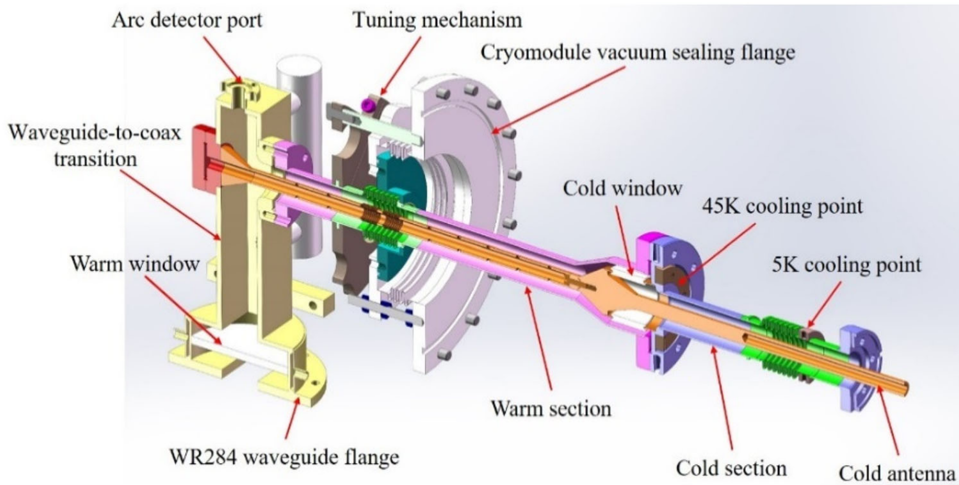

Fig. 1 (Color online) The mechanical design of the SHINE 3.9 GHz fundamental power coupler

copper braid with 5 K and 45 K helium pipes in the third harmonic cryomodule, to increase the cooling capacity of the coupler. The waveguide port of the coupler, connected to a solid-state amplifier (SSA), is selected as the WR284 waveguide, which has a higher power capacity and is easier to manufacture than the WR229 waveguide.

Unlike the 1.3 GHz accelerating cavity, the third harmonic cavity is in the deceleration phase instead of the acceleration phase. Most of the power comes from the beam; thus, the power fed by the SSA is significantly reduced. The external quality factor of the superconducting cavity and the power requirements can be calculated using Eqs. (1)–(3), and are related to the beam current and other parameters, such as the coupling coefficient β, beam current I_b, cavity intrinsic quality factor Q_0, cavity voltage V_c, R/Q of the cavity, frequency detuning δf, and resonant frequency f_0 [17]. For the SHINE project, the optimal external quality factor is 2.13×10^7, for the following working conditions: the final average beam current in Linac is 0.3 mA, the nominal accelerating gradient E_{acc} of the 3.9 GHz superconducting cavity is 13.1 MV/m, the cavity intrinsic quality factor Q_0 is 2.0×10^9, the beam-cavity phase Φ is at 153°, and the frequency detuning δf caused by the peak microphonics effect is 30 Hz. The RF power induced by a beam and radiated to the coupler is approximately 1.36 kW per cavity, and the required input power from the SSA for maintaining the operating gradient is approximately 0.2 kW. Thus, the coupler should be rated for ~ 1.8 kW of average RF power. Therefore, the 3.9 GHz coupler is designed to withstand the CW power of 2 kW in the TW mode. Figure 2 shows the generator power, the radiation power of the cavity, and the total coupler's power capability, for different beam currents. The maximal generator power does not exceed 0.5 kW, considering the waveguide transmission loss of ~ 15%.

The external quality factor of the cavities will be adjusted to the optimal value after the cryomodule is cooled down to 2 K, and it will be maintained during the accelerator operation. To achieve the optimal external quality factor, the SHINE 3.9 GHz fundamental power coupler is designed as an adjustable structure. Through the tuning mechanism of the warm section, the stretching of the bellows can be controlled, to change the insertion depth of the antenna into the cavity, thereby achieving coupling adjustability. The adjustment range of the antenna is about ± 3 mm, so that the external quality factor can be varied from 1.0×10^7 to 5.0×10^7, increasing the external quality factor adjustment capacity up to fivefold.

$$\beta_{opt} = \left[\left(1 + \frac{I_b Q_0 (R/Q)}{V_c}\right)^2 + \left(\frac{2Q_0 \delta f}{f_0}\right)^2\right]^{1/2} \tag{1}$$

$$Q_e = Q_0/\beta_{opt} \tag{2}$$

$$P_g = \frac{V^2}{4\left(R/Q\right)Q_1}\left[\left(1 + \frac{I_b\left(R/Q\right)Q_1}{V_c}\cos\emptyset\right)^2 + \left(2Q_1\frac{\delta f}{f} + \frac{I\left(R/Q\right)Q_1}{V}\sin\emptyset\right)^2\right] \tag{3}$$

3 RF simulations and optimization

3.1 Simulation and optimization of the cold section

All components of the 3.9 GHz coupler, including the cold section, the warm section, the waveguide-to-coax transition, and the bellows section, were optimized using the high-frequency simulation software CST [18]. The goal

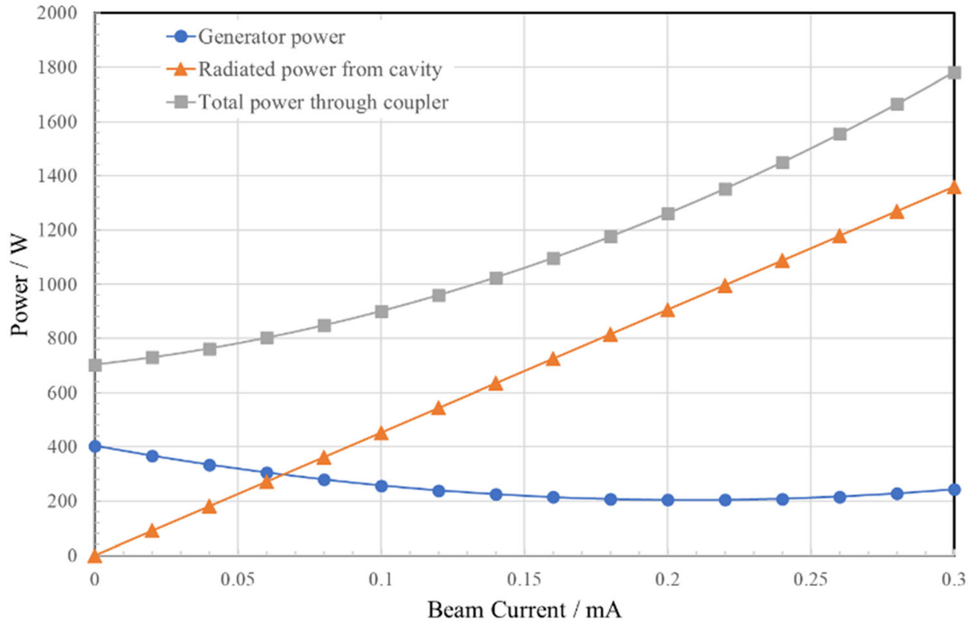

Fig. 2 Generator power, radiated power, and total power, vs. the beam current

of the S-parameter optimization was to make the reflection coefficient as small as possible and the transmission coefficient as large as possible, at the operating frequency. The requirements are that S11 and S21 for the 3.9 GHz coupler should be better than − 21 dB and − 0.2 dB separately. The cold ceramic window of the 3.9 GHz coupler uses a cylindrical window type, which is similar to the cold window structure of the SHINE 1.3 GHz fundamental power coupler. The cold section of the coupler consists of a 50-Ohm-resistance coaxial line with a 30-mm-diameter outer conductor. Figure 3 shows the three-dimensional (3D) model of the cold section and its instant electromagnetic field distribution in the TW mode. The transmission coefficient is related to the size of the structure. First, we scanned and optimized each size parameter of the structure and finally combined them together for the final optimization. Figure 4 shows the frequency dependence of the S11 and S21 parameters, for different radii of the cold window's outer conductor. The S-parameter values were the best when the radius of the cold window's outer conductor was 28 mm. Using this method, we determined the dimensions of the other structural parameters. Figure 5 shows the S-parameter curves for the optimized cold section, for the 3.4–4.4 GHz frequency range. The optimal transmission coefficient S21 ≈ − 0.0055 dB and the reflection coefficient S11 = − 35 dB of the cold section at the 3.9 GHz frequency were obtained.

3.2 Simulation and optimization of the warm section and the waveguide-to-coax transition

The warm window structure of the 3.9 GHz coupler was based on the window structure of the klystron, which uses a flat disk ceramic. The waveguide-to-coax transition adopted the WR284 waveguide structure. To convert the transverse electric (TE) mode of the waveguide into the transverse electromagnetic (TEM) mode of the coaxial line, a conical transition structure was added to the warm section. Meanwhile, the diameter of the warm ceramic window must be larger than the length of the diagonal of the waveguide cross-section, to minimize the electric field intensity at the center of the ceramic. The thickness of the warm ceramic window must also be carefully considered. It should not be too thin; otherwise, the mechanical strength will be insufficient; at the same time, it should not be too thick, as the microwave loss will increase. The optimal S-parameters were obtained by scanning various size parameters of the warm window and the waveguide-to-coax transition. Figure 6 shows the 3D model of the warm section and the waveguide-to-coax transition and its instant electromagnetic field distribution in the TW mode. Figure 7 shows the optimal S-parameter curves of the warm section and the waveguide-to-coax transition in the 3.4–4.4 GHz frequency range. The optimal transmission coefficient S21 ≈ − 0.00067 dB and the reflection coefficient S11 = − 30.9 dB of the warm section and of the waveguide-to-coax transition at the 3.9 GHz frequency were obtained.

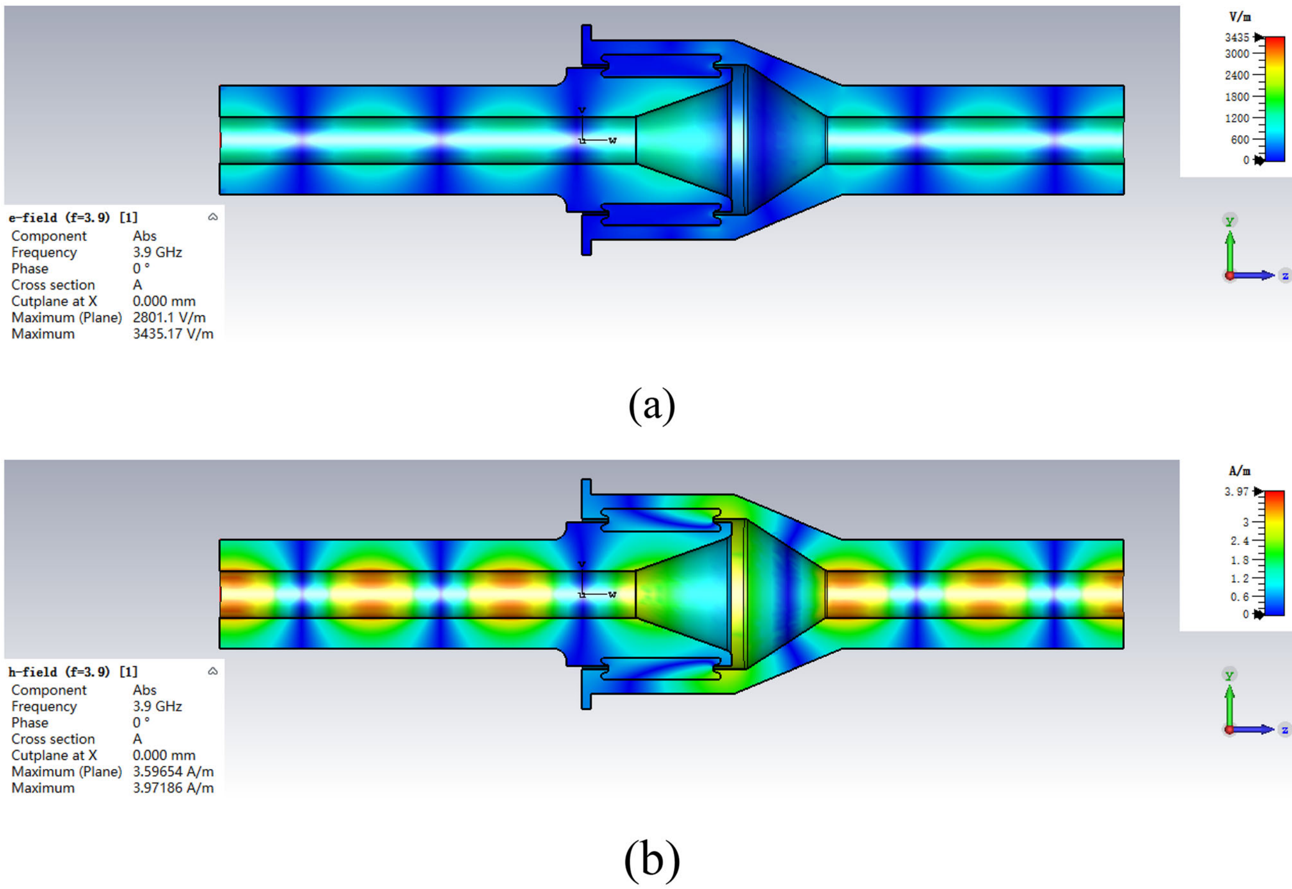

Fig. 3 (Color online) The model of the cold section and its instant electric (**a**) and magnetic (**b**) field distributions

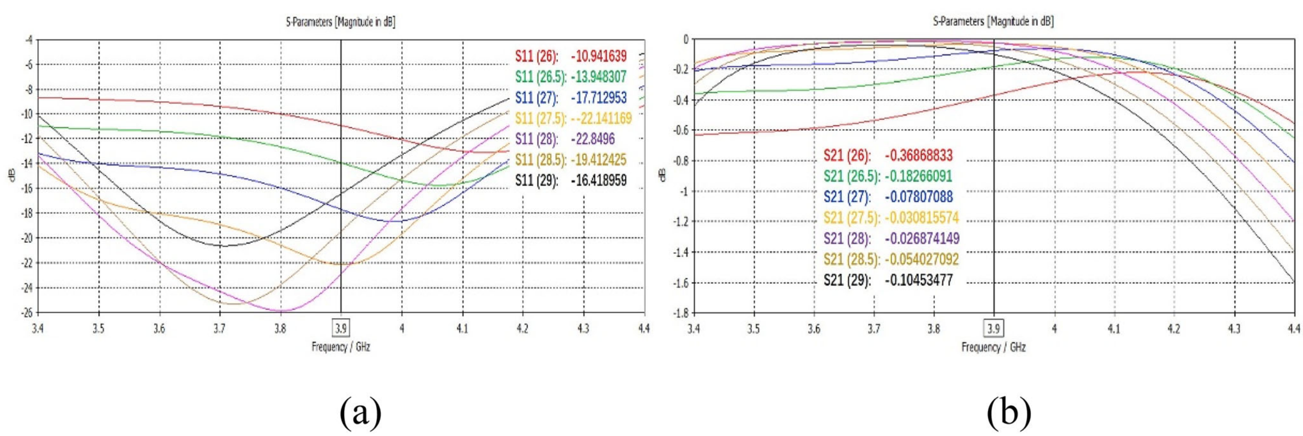

Fig. 4 S11 (**a**) and S21 (**b**) parameter curves vs. frequency, for different radii of the cold window's outer conductor

3.3 Simulation and optimization of the bellows

The structure and the size of the bellows used in the 3.9 GHz coupler should be considered carefully. On the one hand, its deformation is required for meeting the adjustment requirement of ± 3 mm and easy manufacturing; on the other hand, it is necessary to achieve better power transmission. By scanning different structure size parameters of the warm section bellows, the optimal S-parameters were obtained. Figure 8 shows the optimized

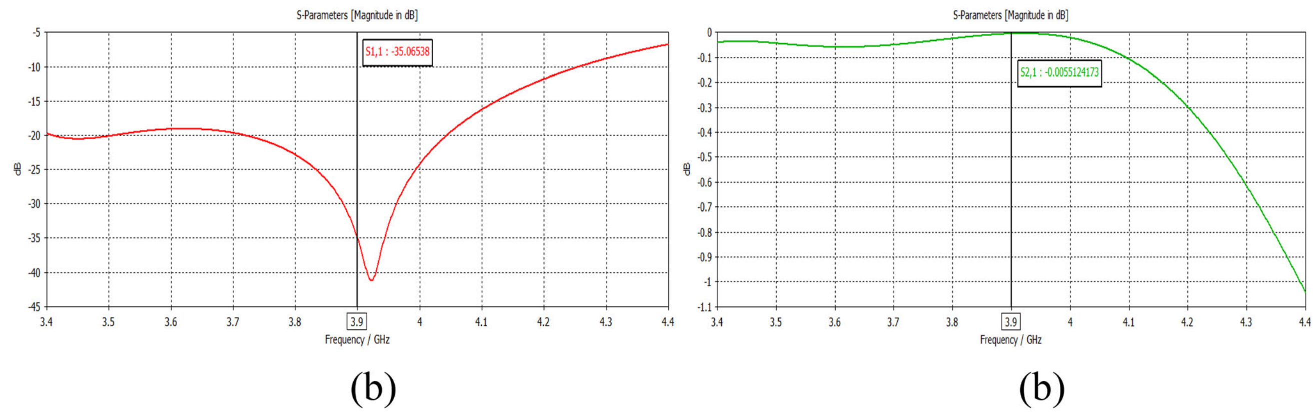

Fig. 5 S11 (**a**) and S21 (**b**) parameter curves vs. frequency, for the optimized cold section

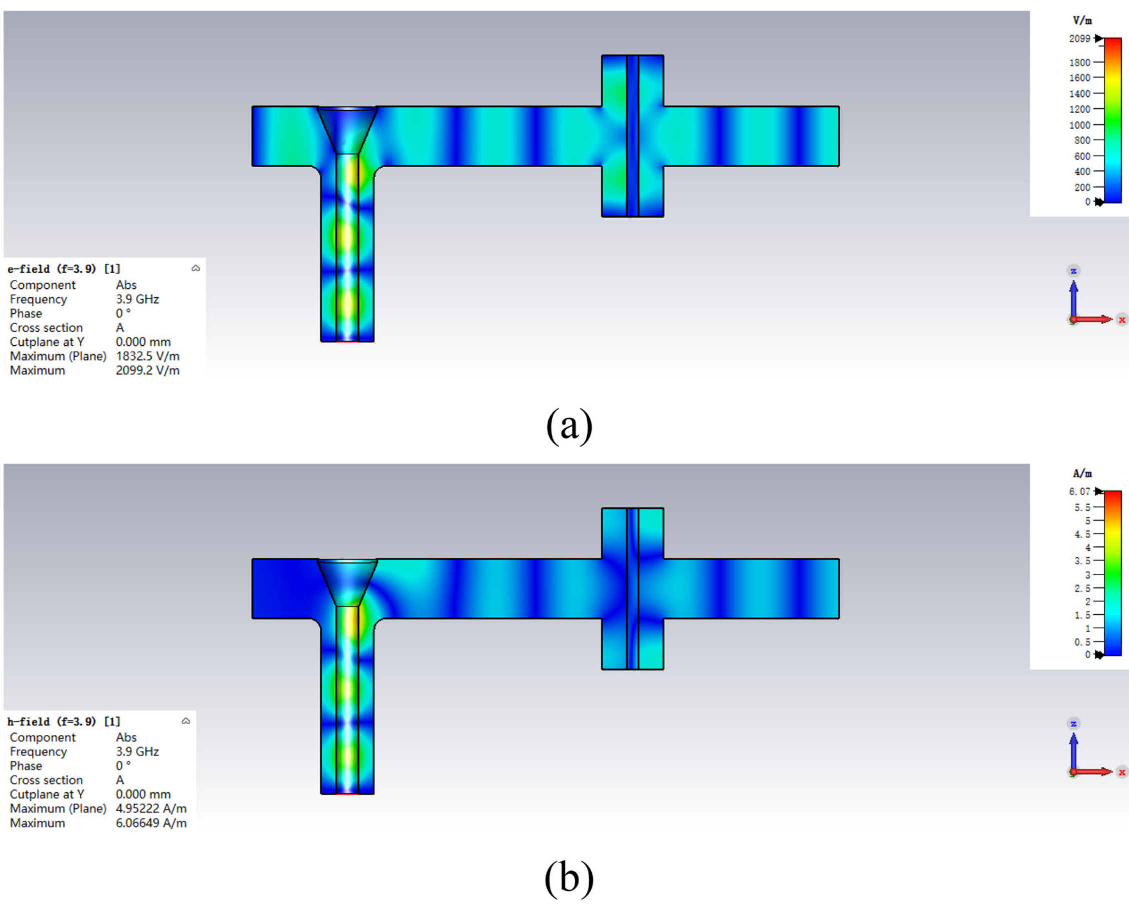

Fig. 6 (Color online) The model of the warm section and the waveguide-to-coax transition, and its instant electric (**a**) and magnetic (**b**) field distributions

structural model of the bellows. Figure 9 shows the optimal S-parameter curves of the bellows in the 3.4–4.4 GHz frequency range. The optimal transmission coefficient S21 ≈ -0.003 dB and the reflection coefficient S11 $= -56.2$ dB of the warm section bellows at the 3.9 GHz frequency were obtained.

3.4 Simulation and optimization of the 3.9 GHz coupler

By combining the optimized cold section, the warm section, and the waveguide-to-coax transition, the optimal S-parameters of the 3.9 GHz coupler with minor structural size changes were obtained. Figure 10 shows the 3D model

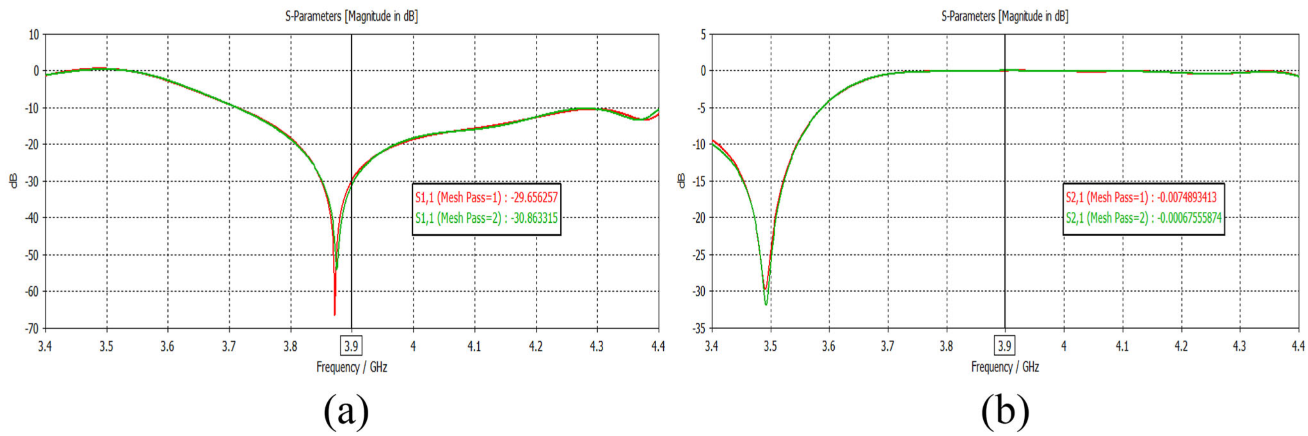

Fig. 7 S11 (**a**) and S21 (**b**) parameter curves of the optimized warm section and the waveguide-to-coax transition, vs. frequency

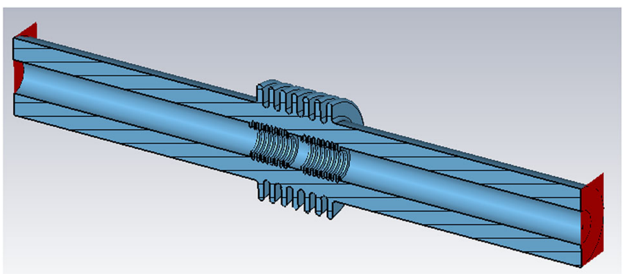

Fig. 8 (Color online) The model of the bellows for the warm section

of the 3.9 GHz coupler and its instant electromagnetic field distribution in the TW mode. Figure 11 shows the optimal S-parameter curves for the 3.9 GHz coupler in the 3.4–4.4 GHz frequency range. After careful selection of the coupler geometry and the materials, the optimal reflection coefficient S11 = − 27.6 dB and the transmission coefficient S21 = − 0.05 dB at the 3.9 GHz frequency were obtained. These satisfied our requirements, that is, the requirements are that S11 and S21 for the 3.9 GHz coupler should be better than − 21 dB and − 0.2 dB separately.

3.5 Simulation and calculation of the external quality factor

The external quality factor Q_{ext} characterizes the degree of power coupling between the superconducting cavity and the fundamental power coupler [19]. The geometry of the antenna tip of the cold section influences the external quality factor, and it is necessary to confirm it before deciding the optimal Q_{ext}. Figure 12 shows the geometry of the antenna tip of the cold section. The antenna adopts a hollow structure, for reducing the mechanical stress on the cold ceramic window. The radius of the hollow hole (R) and the radius of the antenna tip chamfer (r) both affect the external quality factor. Some results were obtained from simulations, as follows:

(1) When the radius of the antenna tip chamber changes from 0.1 mm to 0.5 mm, the external quality factor Q_{ext} changes by $\sim$ 2.7%, as shown in Fig. 13a.

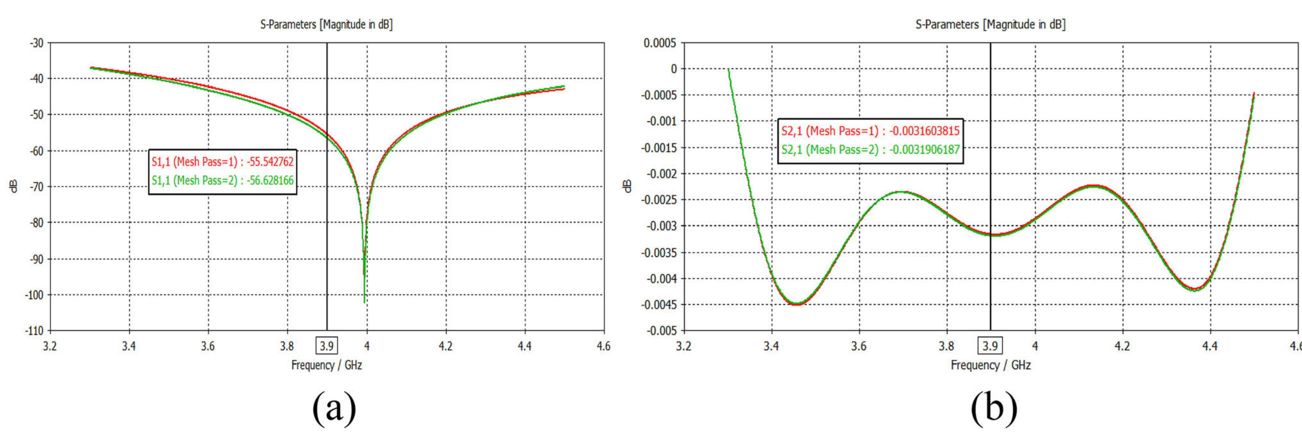

Fig. 9 S11 (**a**) and S21 (**b**) parameter curves of the optimized warm section bellows, vs. frequency

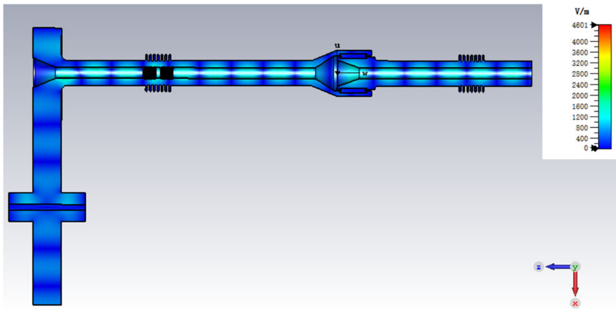

(a)

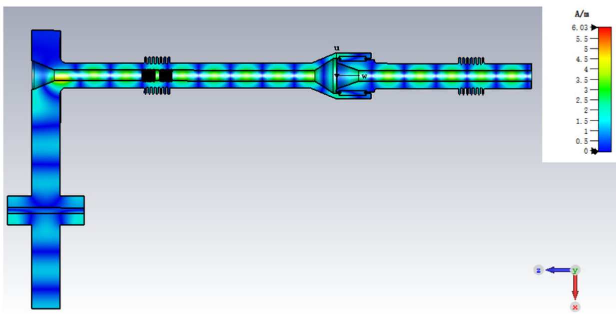

(b)

Fig. 10 (Color online) The model of the 3.9 GHz coupler and its instant electric (**a**) and magnetic (**b**) field distributions

(2) When the radius of the antenna's hollow hole changes from 3 to 6 mm, the external quality factor Q_{ext} changes by $\sim$ 14%, as shown in Fig. 13b.

(3) When the height of the antenna's hollow hole (h) changes from 31.75 to 36.75, the external quality factor Q_{ext} changes by $\sim$ 0.36%, which has little effect on Q_{ext}. This effect can be ignored.

The final geometry of the antenna tip of the cold section was determined by compromising the calculation results and machining capability. The radius of the antenna's hollow hole was set to 5 mm, the height of the hollow hole was set to 36 mm, and the radius of the antenna tip chamber was set to 0.5 mm. Then, the external quality factor of the 3.9 GHz 9-cell cavity could be calculated for different antenna insertion depths. Figure 14 shows the external quality factor Q_{ext} curve for the 3.9 GHz 9-cell cavity in relation to the position of the antenna from the cavity axis. When the distance between the antenna tip and the cavity axis changes from 24 to 30 mm, Q_{ext} varies from 1.0×10^7 to 5.0×10^7.

3.6 The position of the cold window in the standing-wave mode

There are two situations where the coupler works in the standing-wave mode: (1) when the fundamental power couplers are off-resonance (cavities not tuned) high-power conditioning after assembly into the cryomodule, and (2) when there is no beam current, but the cavity should maintain the accelerating gradient, and thus most or all of the input power will be reflected from the cavity. The input RF power is approximately 1 kW and 0.35 kW, respectively, in both cases for the 3.9 GHz fundamental power coupler. The ceramic window is usually placed at the standing-wave electric field node to reduce the damage to the ceramic window. Because the cold window of the 3.9 GHz coupler is a cylindrical ceramic window, and because the electric field is concentrated at its two ends, it is hoped that the two ends of the cylindrical ceramic window are placed as close as possible to the node of the standing-wave electric field. Here, we only considered the most extreme case; that is, the case of the off-resonance high-power conditioning of the coupler when the superconducting cavity is detuned. By adjusting the length of the

Fig. 11 S-parameter curves of the optimized 3.9 GHz power coupler, vs. frequency

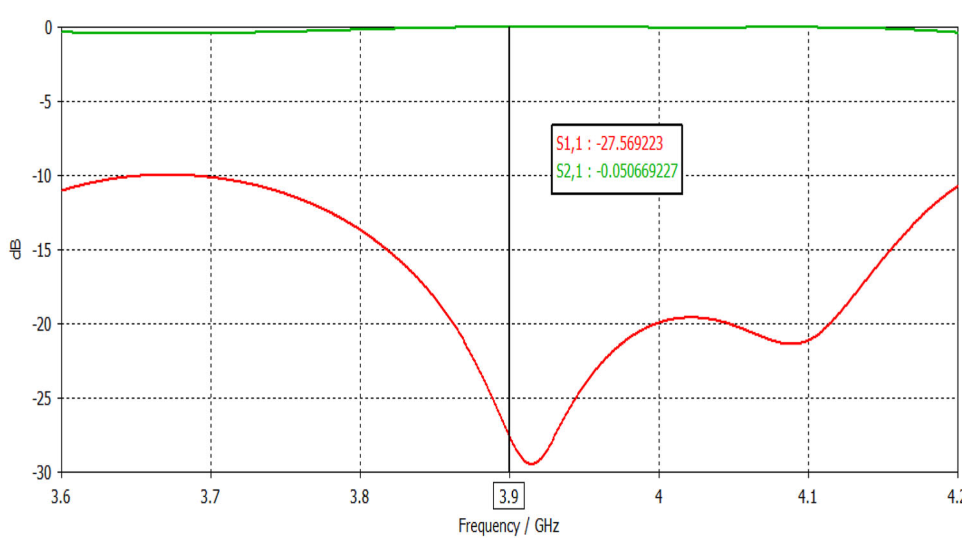

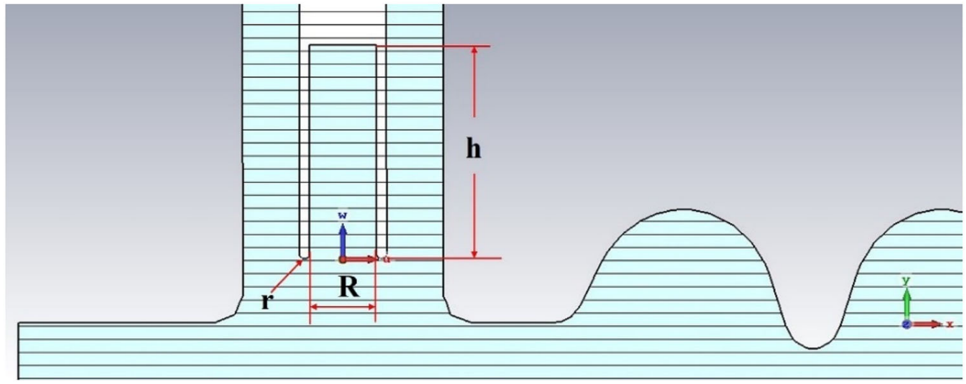

Fig. 12 (Color online) The geometry of the cold section's antenna tip

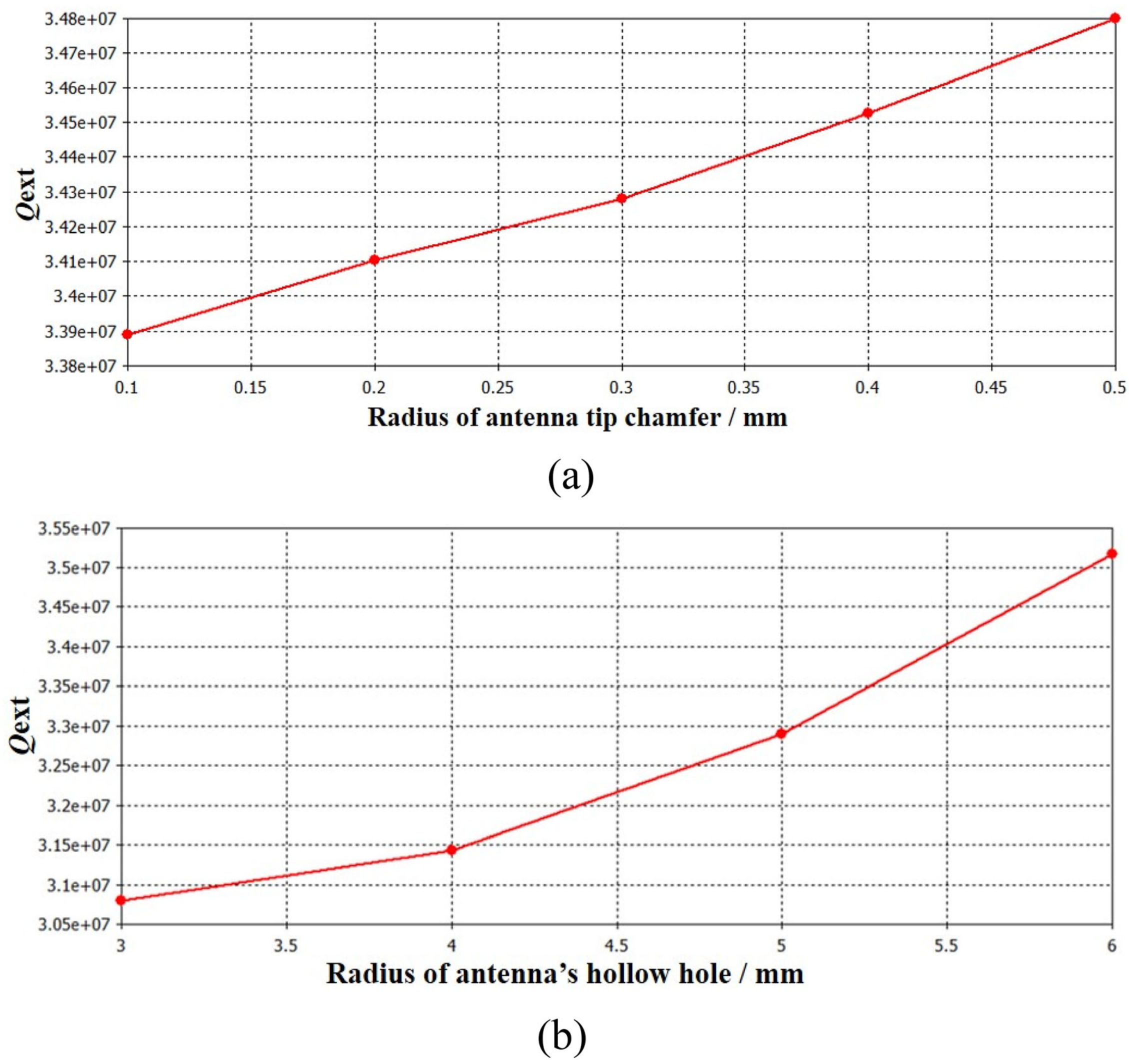

Fig. 13 The dependences of Q_{ext} on (**a**) the radius of the antenna tip chamber and (**b**) on the radius of the antenna hollow hole

cold section of the coupler, the two ends of the cold ceramic window were positioned at the minimum of the standing-wave electric field. Figure 15 shows the instantaneous standing-wave electric field distribution of the 3.9 GHz coupler when the cavity is off-resonance. Figure 16 shows the relationship between the position of the cold window and the standing-wave electric field intensity. Evidently, the two ends of the cold ceramic window are at the weak standing-wave electric field loci.

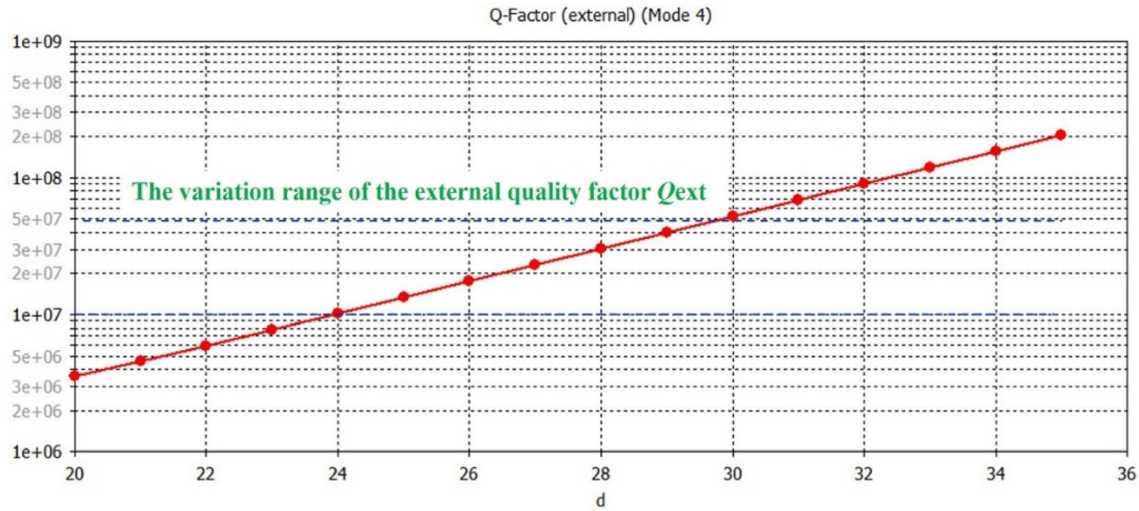

Fig. 14 (Color online) The relationship between Q_{ext} of the 3.9 GHz 9-cell cavity and the distance between the antenna tip and the cavity axis

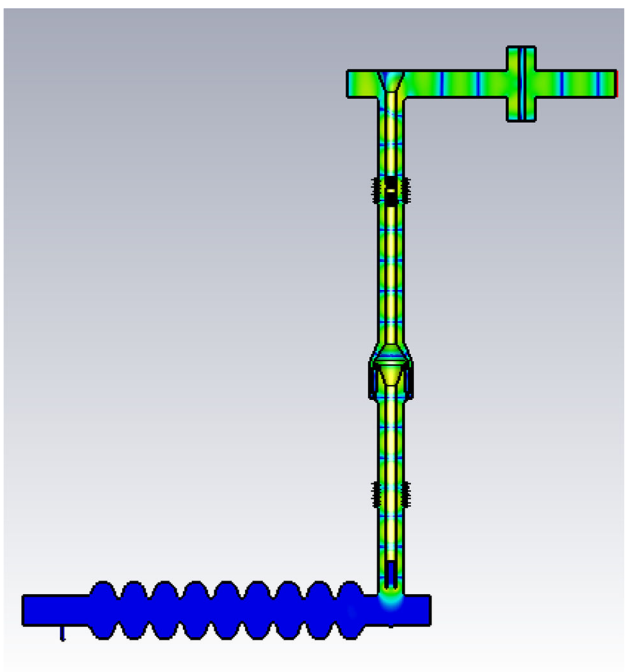

Fig. 15 (Color online) The instantaneous standing-wave electric field distribution of the 3.9 GHz coupler and the cavity

4 Multipacting simulations of the cold section

Secondary electron multipacting is a common resonant effect between electrons and high-frequency electromagnetic fields in vacuum microwave devices, such as power couplers and superconducting cavities [20, 21]. The underlying physical process is generally described as follows: some free electrons in vacuum microwave devices are produced owing to cosmic rays, the photoelectric effect, field emission, and other mechanisms. These free electrons collide with the surface of the device under the action of a high-frequency electromagnetic field, and one or more secondary electrons are ejected from the surface of the device. The number of secondary electrons is directly related to the SEC of the surface material and the impact energy of the free electrons. These secondary electrons are also accelerated or decelerated by the high-frequency electromagnetic field, bombarding the surface of the device again, and new secondary electrons may be ejected. When the flight trajectory of the electrons returns to the starting point or its vicinity after the integer multiple of the microwave period and the SEC of the surface exceeds 1, the number of electrons increases exponentially. The accelerated electrons bombard the surface of the device, causing surface heating and damage, and the vacuum deteriorates owing to the desorbed gas, which is one of the main factors that limit the operating power of the couplers.

It is almost impossible to design a coupler that has no multipacting throughout the entire range of power values, but in practice multipacting can be alleviated in the operational power range. Selecting the appropriate coaxial line size and characteristic impedance of the coupler, or changing the resonance mode of the secondary electrons by applying a bias voltage between the inner and outer conductors or adding an external deflection magnetic field are some conventional methods for avoiding and/or suppressing multipacting in the operational power range. Sometimes, multipacting disappears after high-power conditioning, and the corresponding vacuum becomes better. Multipacting that does not disappear with high-power conditioning is called structural multipacting. Structural multipacting should be avoided by careful design.

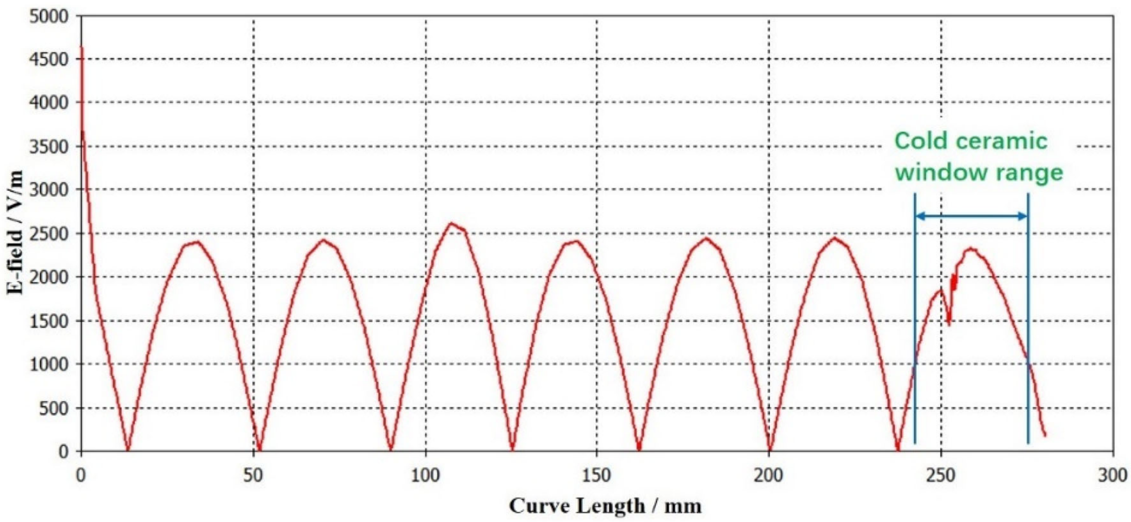

Fig. 16 The relationship between the position of the cold window and the standing-wave electrical field intensity

We used a two-dimensional (2D) simulation program, MultiPac 2.0, jointly developed by Rolf Nevanlinna (Finland) and the DESY team (Germany), to simulate multipacting in axisymmetric RF structures, such as ellipsoidal cavities, coaxial couplers, and other high-frequency devices [22]. Because multipacting in general does not occur in atmospheric environments, here we only focused on the multipacting simulations of the cold section. Figure 17 shows the 2D model of the cold section and its electromagnetic field diagram.

The multipacting simulation of the cold section was first carried out in the TW 0–1000 kW power range, to determine the power level at which the structure exhibits multipacting. In this simulation, the material of the inner and outer conductors was oxygen-free copper, and the cold window material was an alumina ceramic. The secondary electron emission yields of the three different materials are presented in Fig. 18. Figure 19 shows the results of the three important parameters that characterize the multipacting effect in relation to the input power. From top to bottom, they are: (1) the statistics of the number of initial electrons, (2) the average collision energy of the last collision, and (3) the ratio of the remaining electrons to the initial electrons after 20 collisions. It can be seen from the e20/C0 graph in Fig. 19 that the ratio of the number of secondary electrons to the number of initial electrons in the 40–45 kW range and at 785 kW is above 1, which indicates multipacting on the SSA side of the ceramic window

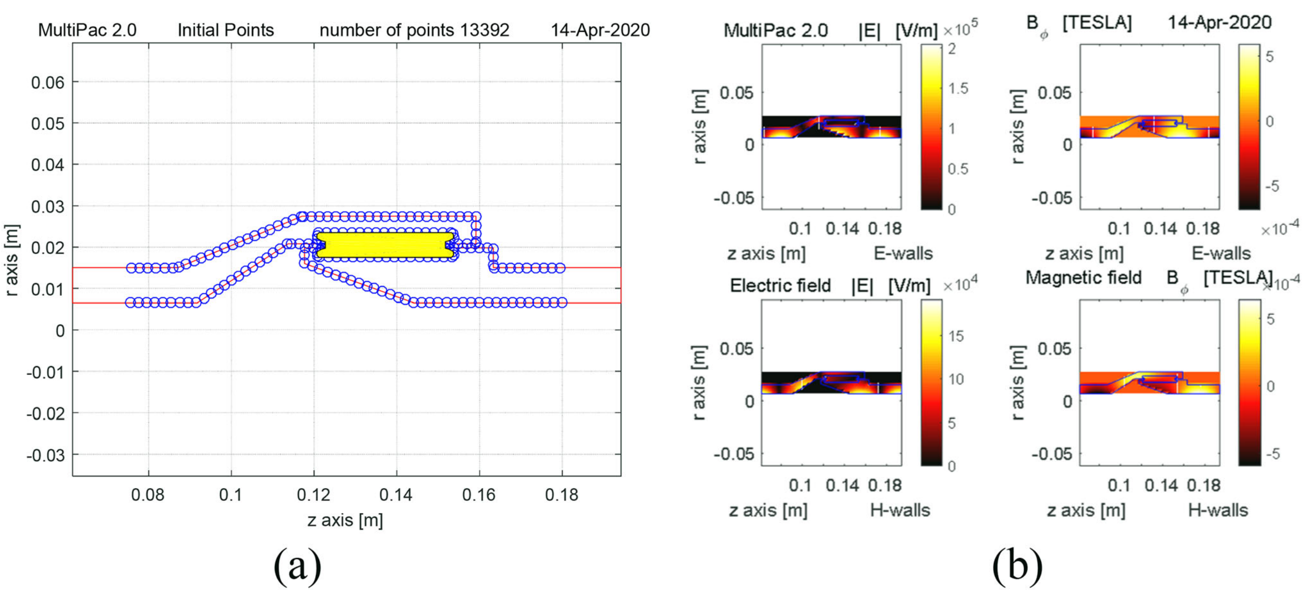

Fig. 17 (Color online) The 2D model of the cold section (**a**) and its electromagnetic field (**b**)

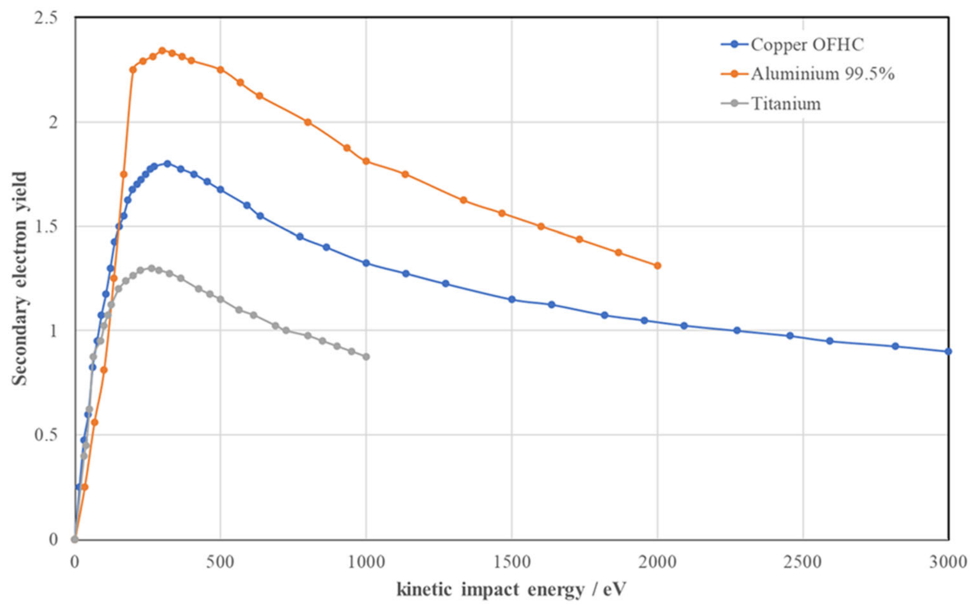

Fig. 18 The secondary electron emission yields of the three different materials

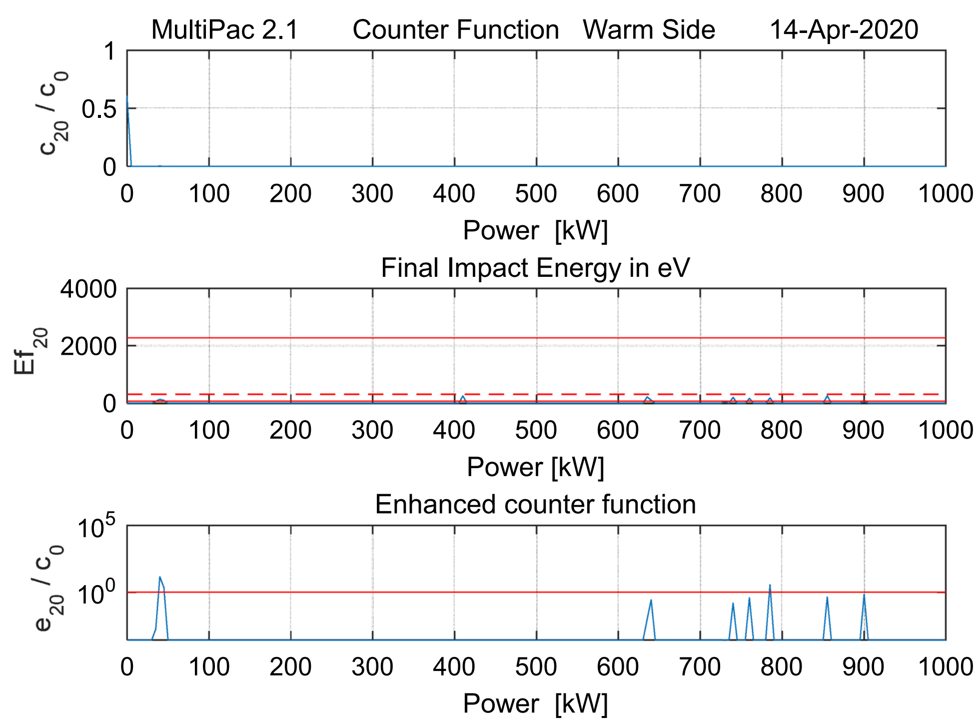

Fig. 19 The input–output ratio of secondary electron emission, for the cold section, for the TW 0–1000 kW power range

in the TW mode. By checking the trajectory of electrons at the 40 kW power level, it was found that there is a two-point first-order multipacting effect between the ceramic window and the copper ring. The electrons form a stable trajectory after more than 20 high-frequency cycles and return to the vicinity of the starting point after each high-frequency cycle, which means that the electrons and the electromagnetic field form a stable first-order resonance. The electrons' trajectories are shown in Fig. 20.

A multipacting simulation of the cold section of the 3.9 GHz coupler in the pure standing-wave mode was also carried out. The locations of the walls were determined using an iterative method and by defining a "stretching area". The default step size in phase was 5°. Simultaneously, the multipacting simulation of the cold section was carried out in the TW 0–5 kW power range, to further verify the geometry of the cold section, as shown in Fig. 21. According to the multipacting simulation of the cold section, the following conclusions were reached:

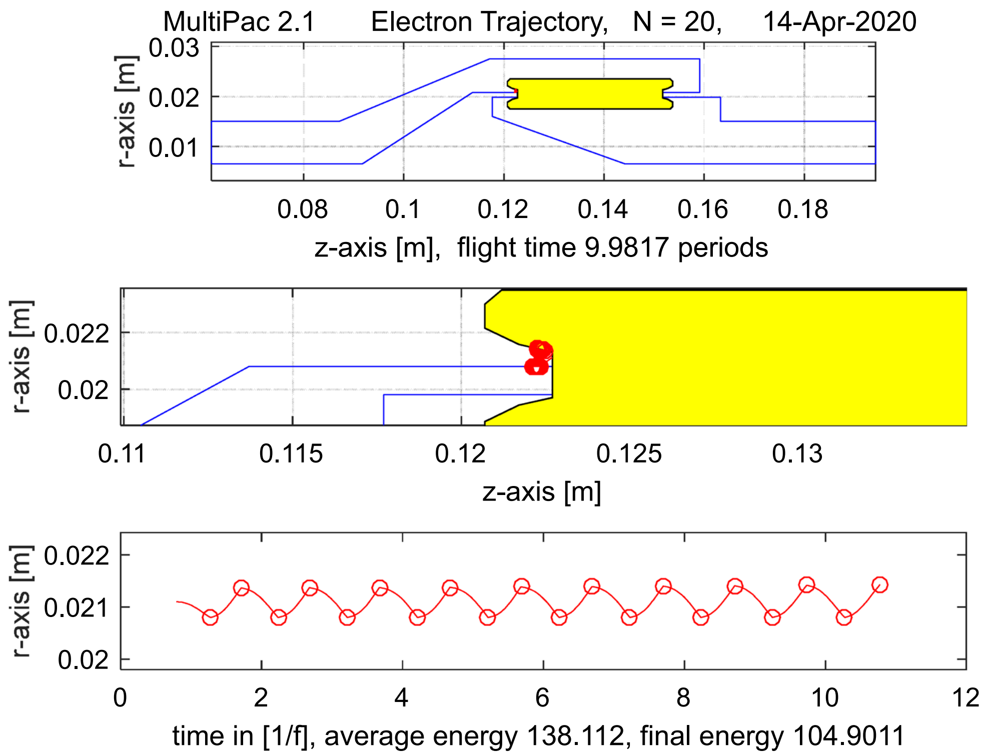

Fig. 20 (Color online) The electrons' trajectories for the cold window, at 40 kW

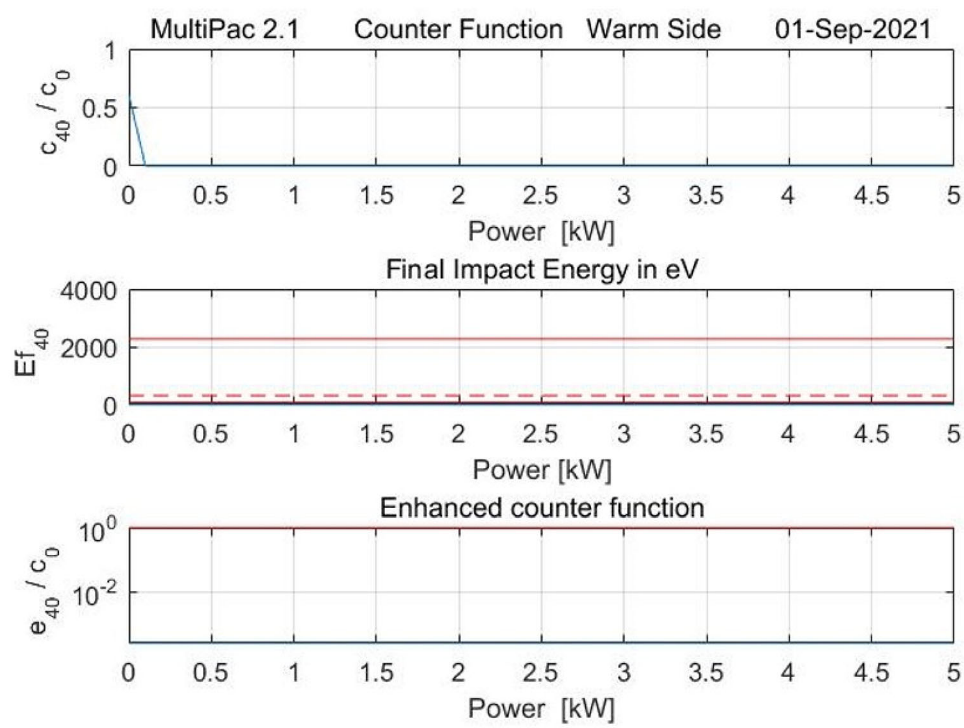

Fig. 21 The input–output ratio of the secondary electron emission for the cold section, in the TW 0–5 kW power range

(1) For the 40–45 kW and 785 kW TW power levels, a two-point, first-order multipacting effect occurred between the groove of the ceramic window and the copper ring on the SSA side of the cold window.

(2) For 630 kW and 880 kW TW power levels, there was a one-point, 16th-order multipacting effect at the outer conductor on the cavity side of the cold window.

(3) For the 35 kW SW power level, there was a two-point, first-order multipacting effect that occurred between the groove of the ceramic and the copper ring on the SSA side of the cold window.
(4) For the cold section of the 3.9 GHz coupler, no structural multipacting was observed at the 2 kW power level.

However, it should be noted that the occurrence of multipacting is a very complex process, and computer simulations have certain limitations and cannot fully reflect reality. However, the simulation results also depend on the real SEC values of the corresponding materials. Simulations can be used for alleviating structural multipacting to the maximal possible extent while designing couplers. At the same time, it is suggested that the vacuum sides of the ceramic window should be coated with a TiN film, for reducing the SEC of the ceramic surface in actual manufacturing [23]. A bias voltage between the inner and outer conductors can be also considered, for destroying the electronic resonance conditions. In addition, ensuring a very clean RF surface of the coupler and clean baking can reduce multipacting.

5 Thermal calculation of the 3.9 GHz coupler

When RF power is transmitted through the coupler, ohmic heat loss on the coupler's RF surface and dielectric heat loss in the ceramic body are generated. Copper electroplating is often performed on the RF surface of stainless steel inner and outer conductors to reduce the RF heat loss [24, 25]. The antenna of the 3.9 GHz coupler cold section is made of oxygen-free copper, and other stainless steel conductors are coated with copper. The thickness of the copper film is carefully controlled, to ensure that the surface temperature of the coupler is in the acceptable range.

A 3D model of the 3.9 GHz coupler was established using the CST software, for thermal calculations; the model is shown in Fig. 22. First, CW RF power at 2 kW was applied to the coaxial port, and the thickness of the copper film on the inner and outer conductors was set to 30 μm in the simulation. Stainless steel 316 L, high-conductivity oxygen-free copper, and ceramic materials were used for the different parts of the coupler. The thermal and electrical conductivity properties of the copper film corresponding to RRR (Residual Resistance Ratio) = 50 were used [26]. The ceramic's properties were $\varepsilon = 9.4$, $\tan\delta = 4 \times 10^{-4}$. The temperature boundaries of the 5 K and 45 K intercept points of the 3.9 GHz coupler were also set, as shown in Fig. 21. Because the coupler maximal temperature of the 3D model including the coaxial-to-waveguide transition increased by approximately 10% compared with the coaxial coupler geometry without the input waveguide [11], we used a coaxial coupler model without a waveguide to speed up the computation in our thermal calculation.

The electromagnetic field distribution under the 2 kW power TW condition was first calculated. Second, the surface temperature of the coupler was calculated based on the microwave loss and dielectric loss. When the thickness of the copper film on the inner and outer conductors was 30 μm, the maximal surface temperature of the coupler was approximately 645 K, as shown in Fig. 23. The coupler temperature should not exceed 450 K, which corresponds to the coupler baking temperature; therefore, extensive surface degassing was prevented, and a manageable vacuum level was ensured [27]. It was necessary to increase the thickness of the copper film on the inner conductor of the warm section, for solving the overheating problem.

Figure 24 shows the relationship between the maximal temperature of the 3.9 GHz coupler and the copper film thickness, for the 2 kW TW power scenario. When the thickness of the copper film on the inner conductor surface of the warm section reached 150 μm, the maximal temperature of the 3.9 GHz coupler was controllably below 350 K (ceramic maximal allowable temperature for normal operation) for the 2 kW TW power. Therefore, the thickness of the copper film for the 3.9 GHz fundamental power coupler was selected as follows: the thicknesses of the copper films on the outer conductor of the cold and warm

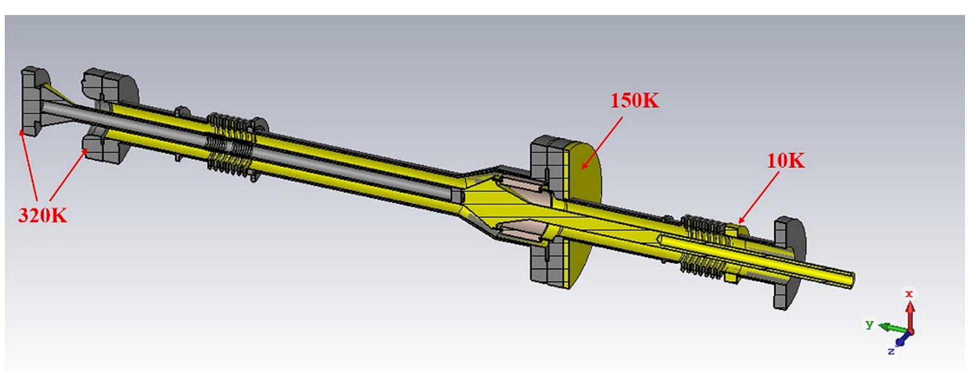

Fig. 22 (Color online) The 3D thermal model of the 3.9 GHz coupler and its thermal boundary conditions

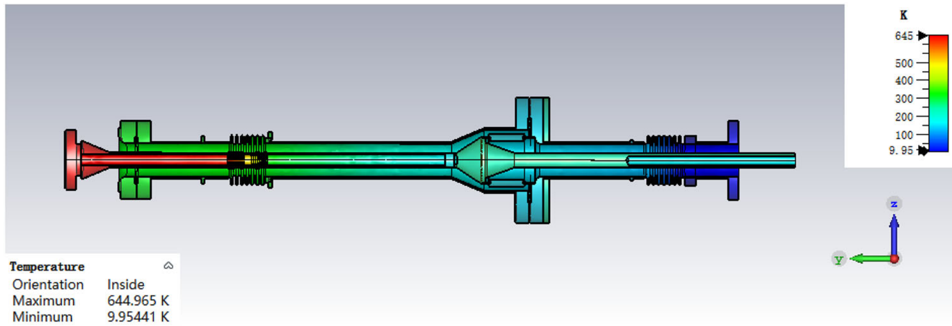

Fig. 23 (Color online) The surface temperature distribution of the 3.9 GHz coupler under the 2 kW TW power (30-μm-thick copper film was coated on the inner and outer conductors)

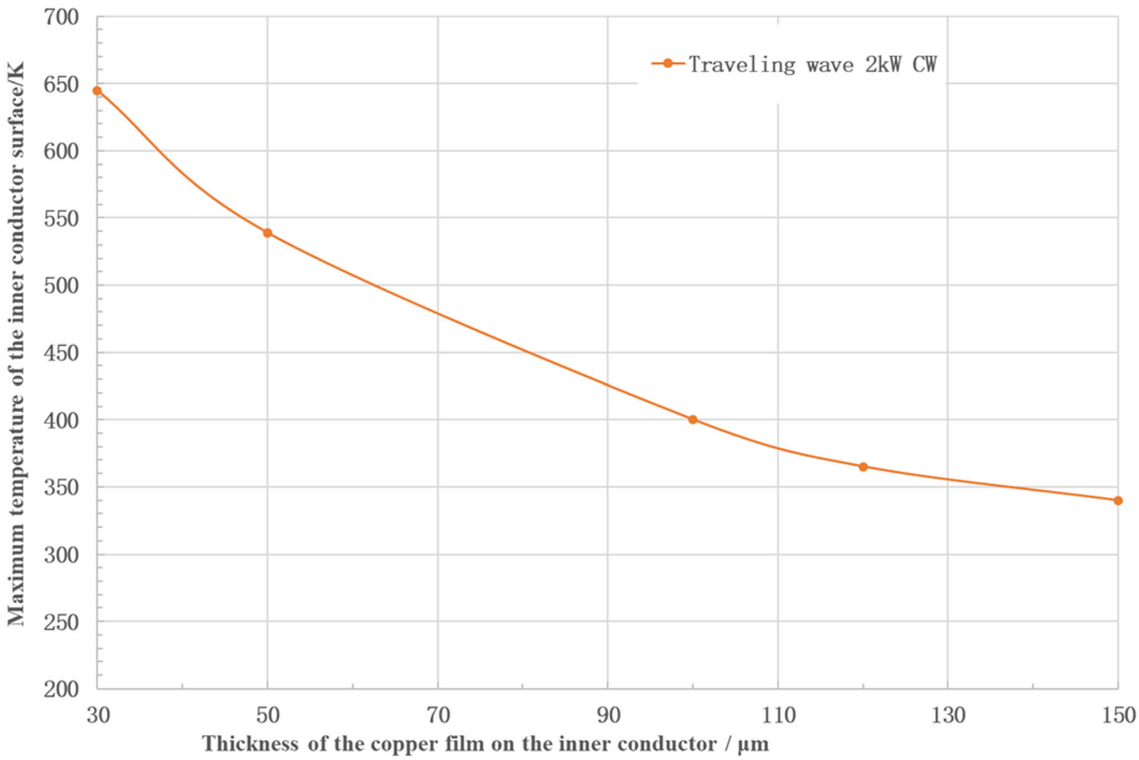

Fig. 24 The relationship between the maximal temperature of the 3.9 GHz coupler and the copper film thickness, for the 2 kW TW power scenario

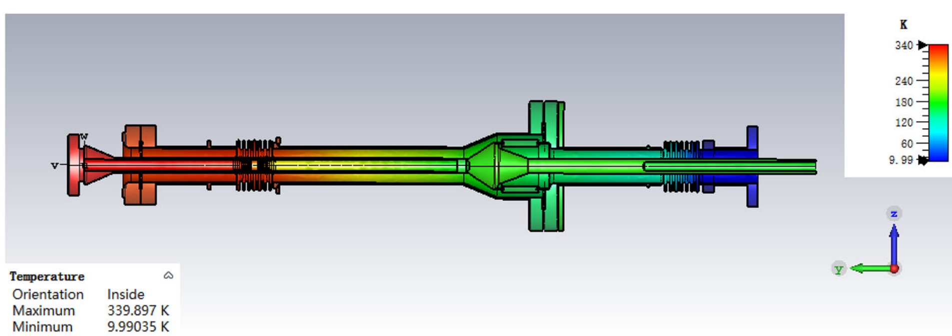

Fig. 25 (Color online) The surface temperature distribution of the 3.9 GHz coupler with a 150-μm-thick copper film on the inner conductor, for the 2 kW TW power scenario

sections were 30 μm, and the thickness of the copper film on the inner conductor of the warm section was 150 μm. Figure 25 shows the surface temperature distribution for the 3.9 GHz coupler with a 150-μm-thick copper film on the inner conductor of the warm section, for the 2 kW TW power scenario. Figure 26 shows the temperature

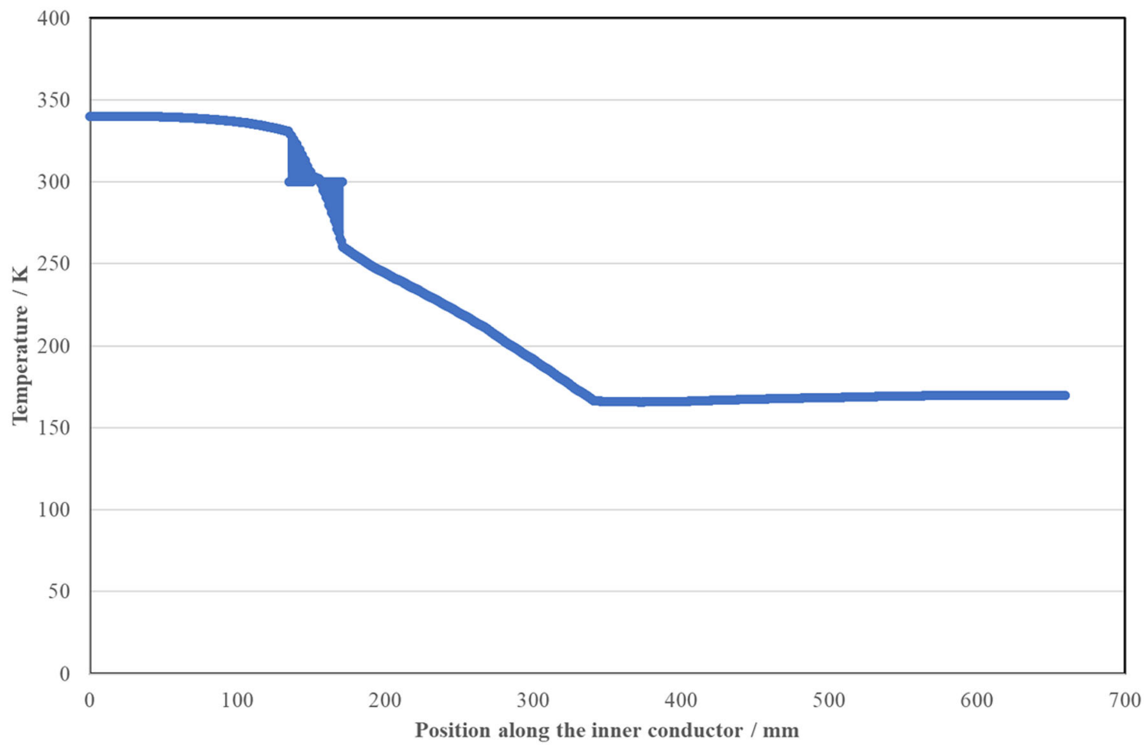

Fig. 26 The temperature distribution along the inner conductor surface of the 3.9 GHz coupler, for the 2 kW TW power scenario

distribution along the inner conductor surface of the warm section. The maximal temperature of the 3.9 GHz coupler was approximately 340 K, satisfying our requirements.

6 Conclusion

The 3.9 GHz fundamental power coupler of the third harmonic cavity for the SHINE project was designed to meet the 2 kW TW power requirements. The geometry of the different subassembly of the 3.9 GHz coupler was optimized using RF simulations. After careful selection of the geometry and the materials, the optimal reflection coefficient of the 3.9 GHz coupler was reduced to − 27.6 dB and the transmission coefficient was only − 0.05 dB. The external quality factor Q_{ext} of the third harmonic cavity varied from 1.0×10^7 to 5.0×10^7 by adjusting the insertion depth of the coupler's cold antenna. No structural multipacting occurred at the 2 kW CW power level for the cold section of the 3.9 GHz coupler, and the cold window was in a position with low electric fields, for reducing the risk of a voltage breakdown. The thickness of the copper film on the inner conductor of the warm section was increased to 150 μm, for solving the overheating problem. The simulation results showed that the optimized coupler design met the SHINE project requirements. Based on this design, the first 3.9 GHz coupler prototype is now being manufactured and is expected to be ready for testing at the beginning of the next year.

Acknowledgements We are grateful to Dr. Rui Zhang, Xiu-Dong Yang, and Yun-Feng Liao of the Aerospace Information Research Institute, CAS for their simulation review and verification of the design optimization in this study. We are also grateful to Dr. Yu-Bin Zhao and Meng Zhang of Shanghai Advanced Research Institute, CAS for discussing the SHINE physics parameters, and we are grateful to Dr. Li-Xin Yin and Sen Sun of Shanghai Advanced Research Institute, CAS for their suggestions on the coupler's structural design.

Author contributions All authors contributed to the study conception and design. Material preparation, data collection and analysis were performed by Zhen-Yu Ma. The first draft of the manuscript was written by Zhen-Yu Ma and all authors commented on previous versions of the manuscript. All authors read and approved the final manuscript.

References

1. C. Feng, H.X. Deng, Review of fully coherent free-electron lasers. Nucl. Sci. Tech. **29**, 160 (2018). https://doi.org/10.1007/s41365-018-0490-1
2. Z.T. Zhao, C. Feng, K.Q. Zhang, Two-stage EEHG for coherent hard X-ray generation based on a superconducting linac. Nucl. Sci. Tech. **28**, 117 (2017). https://doi.org/10.1007/s41365-017-0258-z
3. Z.Y. Zhu, Z.T. Zhao, D. Wang et al., SCLF: an 8-GeV CW SCRF linac-based X-ray FEL facility in Shanghai, in

Proceedings of the FEL2017, Santa Fe, NM, USA (2017). https://doi.org/10.18429/JACoW-FEL2017-MOP055
4. Y.X. Zhang, J.F. Chen, D. Wang, RF design optimization for the SHINE 3.9 GHz cavity. Nucl. Sci. Tech. **31**, 73 (2020). https://doi.org/10.1007/s41365-020-00772-z
5. N. Solyak, I. Gonin, H. Edwards et al., Development of the third harmonic SC cavity at Fermilab. in *Proceedings of the Particle Accelerator Conference*, Portland, OR (US), **2**, 1213–1215 (2003). https://doi.org/10.1109/pac.2003.1289656
6. K. Rothemund, D. Hecht, U. Van Rienen, Calculation of RF properties of the third harmonic cavity, in *Proceedings of 22nd International Linear Accelerator Conference*, Lubeck, Germany (2004).
7. A. Variola, High power couplers for linear accelerators, in *Proceedings of Linear Accelerator Conference*, Knoxville, United States (2006).
8. S. Belomestnykh, Review of high-power CW couplers for superconducting cavities, in *Proceedings of the Workshop on High-Power Couplers for Superconducting Accelerators*, Jefferson Laboratory, Newport Virginia, USA October 2002. OAI: CiteSeerX.psu:10.1.1.597.6843
9. I.E. Campisi, Fundamental power couplers for superconducting cavities. in *Proceedings of the 10th Workshop on RF Superconductivity*, Tsukuba, Japan (2001).
10. J. Li, I. Gonin, T. Khabiboulline et al., Simulations and optimizations of a new power coupler for 3.9-ghz superconducting cavities at Fermilab. in *Proceedings of the LINAC*, Knoxville, Tennessee USA (2006).
11. V. Balakin, 3D simulations of 3.9 GHz Coupler for LCLS-II Project, Fermilab report (2017).
12. N. Solyak, I. Gonin, C. Grimm et al., 3.9 GHz power coupler design and test for LCLS-II project. in *Proceedings of the IPAC2018*, Vancouver, BC, Canada (2018). https://doi.org/10.18429/JACoW-IPAC2018-WEPML022
13. J. Li, N. Solyak, T. Wong, Coupling interaction between the power coupler and the third harmonic superconducting cavity, in *Proceedings of PAC07*, Albuquerque, New Mexico, USA (2007). https://doi.org/10.1109/PAC.2007.4441219
14. J. Li, E. Harms, T. Kubicki et al., RF design and processing of a power coupler for third harmonic superconducting cavities. in *Proceedings of the Particle Accelerator Conference*, Albuquerque, NewMexico, USA, 2265–2267 (2007). https://doi.org/10.1109/PAC.2007.4441218
15. E. Gjonaj, W. Ackermann, T. Lau et al., Coupler kicks in the third harmonic module for the XFEL. in *Proceedings of the Particle Accelerator Conference*, Vancouver, Canada (2009).
16. A. Miura, H. Matsumoto, Development of an S-band RF window for linear colliders. Nucl. Instrum. Meth. Phys. Sect. A **334**(2–3), 341–352 (1993). https://doi.org/10.1016/0168-9002(93)90795-J
17. J. Delayen, N. Merminga, On the optimization of q_{ext} under heavy beam loading and in the presence of microphonics, CEBAF-TN-96-022. May 1996.
18. CST-computer simulation technology. http://www.cst.com.
19. Z.Y. Ma, G.M. Ma, H.T. Hou et al., Evaluation of external quality factor of the superconducting cavity using extrapolation method. Nucl. Sci. Tech. **20**(2), 65–70 (2009)
20. A.S. Dhavale, K.C. Mittal, Multipacting analysis of power coupler for SC cavity. Nucl. Instrum. Meth. Phys. Sect. A **677**, 25–30 (2012). https://doi.org/10.1016/j.nima.2012.01.074
21. P. Yla-Oijala, Electron multipacting in TESLA cavities and input couplers. in *Proceedings of the Particle Accelerators*, vol 63, no 105 (1999).
22. P. Yla-Oijala, *Handbook of MultiPac 2.1 Code*. RNI University of Helsinki, (2001)
23. J. Lorkiewicz, A. Brinkmann, B. Dwersteg et al., Surface TiN coating of TESLA couplers as an antimultipactor remedy. in *Proceedings of the 10th workshop on RF superconductivity*, Tsukuba, Japan (2001).
24. N.P Sobenin, A.A. Krasnov, B. Yu et al., Thermal calculations of input coupler for cornell ERL injector cavities. in *Proceedings of the 9th European Particle Accelerator Conference*, Lucerne, Switzerland (2004).
25. I.V. Gonin, T.N. Khabiboulline, A. Lunin et al., Simulations of 3.9 GHz cw coupler for LCLS-II project. in *Proceedings of the 17th International Conference on RF Superconductivity*, Whistler, BC, Canada (2015). https://doi.org/10.18429/JACoW-SRF2015-THPB005
26. C. Weiren, R. Francesco, Anomalous skin effect and resistive wall heating, LHC Project Note (1995).
27. C. Adolphsen, K. Fant, L. Zenghai et al., Modified TTF-3 couplers for LCLS-II, in *Proceedings of SRF2015*, Whistler, BC, Canada.